N. Zaru, M. Rossi, G. Vacca, and G. Vignoli,
(Pseudo-)3D Inversion of Geophysical Electromagnetic Induction Data by Using an Arbitrary Prior and Constrained to Ancillary Information, ICCSA 2023 Workshops, LNCS 14111, pp. 624–638, 2023.

The publisher's version is available at:

https://doi.org/10.1007/978-3-031-37126-4_40

(Pseudo-)3D Inversion of Geophysical Electromagnetic Induction Data by Using an Arbitrary Prior and Constrained to Ancillary Information

Nicola Zaru[1], Matteo Rossi[2], Giuseppina Vacca[1][0000-0001-8161-7667], and Giulio Vignoli[1,3][0000-0002-3437-5826]

[1] University of Cagliari, Cagliari, 09124, Italy
[2] Lund University, Lund, 22100, Sweden
[3] GEUS, Aarhus, 8000, Denmark
gvignoli@unica.it

Abstract. Electromagnetic induction (EMI) methods are often used to map rapidly large areas with minimal logistical efforts. However, they are limited by a small number of frequencies and by their severe ill-posedness. On the other hand, electrical resistivity tomography (ERT) results are generally considered more reliable, with no need for specific calibration procedures and easy 2D/3D inversion. Still, ERT surveys are definitely more time-consuming, and, ideally, an approach with the advantages of both EMI and ERT would be optimal. The present research addresses this issue by incorporating realistic constraints into EMI inversion, going beyond simplistic spatial constraints like smooth or sharp regularization terms, while taking into consideration the ancillary information already available about the investigated site. We demonstrate how additional pre-existing information, such as a reference model (i.e., an existing ERT section) can enhance the EMI inversion. The study verifies the results against observations from boreholes.

Keywords: Electromagnetic Induction, Spatially Constrained Inversion, Realistic Prior Distribution.

1 Introduction

Geophysical techniques refer to (quasi-)non-invasive methods employed to infer the physical properties of the subsurface. Among these techniques, electrical resistivity tomography (ERT) and electromagnetic induction (EMI) are frequently used to recover the electrical characteristics - mainly, the electrical resistivity - of the medium.

ERT data are collected through a series of electrodes galvanically coupled to the ground. Nowadays, ERT data are routinely inverted with 2D/3D forward modeling. Conversely, EMI measurements can be collected without any physical contact with the surface, and, in most cases, the data are inverted via simple 1D forward modeling. Hence, the collection of ERT data generally requires much more effort than the acquisition of EMI measurements [1, 2] because of the necessity for the electrodes' direct contact with the ground. On the other hand, EMI methods can be used to reconstruct the 3D resistivity volume of extremely large areas in a very limited amount of time; in this respect, there even exist EMI systems designed to be mounted on helicopters/airplanes [3-6]. Despite being more troublesome to collect than EMI observations, ERT measurements do not need special calibration procedures as their observations can be readily checked against test resistances [7-11]. In addition, the capability of 2D/3D inversion contributes to the reduction of artifacts due to the unavoidable presence of coherent noise (i.e.: the modelling error). However, modelling error will always be present (even sophisticated 3D tools are mere approximations of real phenomena) and it should be taken into account to avoid misleading overinterpretation of the data. Clearly, the standard, simplistic, 1D strategies adopted for the EMI inversion are more prone to be negatively affected by this kind of coherent noise [12, 13].

In another respect, to enforce some level of spatial coherence between the 1D inversion results and, in this way, contribute further to tackling effectively the ill-posedness of the problem, regularization terms acting both vertically and laterally have been utilized during the inversion of large EMI datasets. Over the years, various options for both lateral and vertical regularization terms have been investigated and implemented: in addition to the commonly used L2-norm - which promotes solutions that minimize the spatial variation of the model parameters [14-16] - other stabilizer terms, such as the Minimum Support (MS) stabilizer, have gained popularity [17-21]. The MS stabilizers favor the selection of solutions characterized by abrupt resistivity changes, and this, in many cases, might better reflect the investigated geologies. Similar arguments apply to the ERT inversion: also in this case, several stabilizers have been proposed to address the severe ill-posedness of the problem and to correctly formalize the available a priori information [22-26].

The newest deterministic approaches, based on the minimization of Tikhonov's objective function and formalizing the a priori information via the regularization terms, are still quite successful in exploring the solution space [27]. However, probabilistic approaches are becoming more and more frequent as they are capable of assessing the solution uncertainty in a very natural way and of being fed with arbitrary (realistic) prior [28-30].

For the specific field dataset investigated here, we needed a pragmatic strategy capable: 1) of incorporating realistic prior distribution ensuring that the individual 1D EMI reconstructions were compatible with specific expectations about the studied subsurface (so, not, simply, blocky or smooth vertical resistivity models) and 2) of guaranteeing that, laterally, the solutions were consistent with the pre-existing knowledge of the site (i.e., alternatively: a previous 2D ERT section or its corresponding 2D geological interpretation).

2 Methodology

The aim of this research is to incorporate as much prior information as possible into the inversion of EMI datasets. Electromagnetic data are typically acquired with some ideas of the pursued target or with other geophysical measurements available. In this study, the EMI data are inverted by making use of the ERT results (either directly or through their interpretations) obtained along a single acquisition line crossing the investigated area. The objective is to spread the information from the ERT 2D section throughout the entire 3D volume of the EMI survey.

EMI inversion is extremely ill-posed due to the limited number of observations, noise in the data (caused, for example, by unwanted inclinations of the instrumentation), and the nonlinearity of the forward modelling. So, in a deterministic inversion, some level of regularization is required to get a unique and stable solution. Regularization picks the unique and stable solution amongst all possible models fitting the data within the level sets by the estimated noise in the data. In most cases, the regularization is enforced via the minimization of the stabilizer

$$s(\boldsymbol{m}) = \left\|\boldsymbol{m} - \boldsymbol{m}_{apr}\right\|, \tag{1}$$

in which: $\boldsymbol{m}$ is the vector of the model parameters - in this specific case, the resistivity of each layer - and $\boldsymbol{m}_{apr}$ is a reference model.

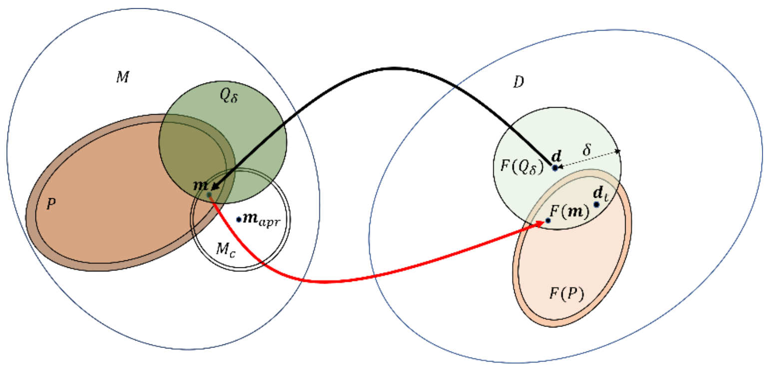

Fig. 1. $\boldsymbol{d}$ is the measurements' vector consisting of the summation of the true data vector $\boldsymbol{d_t}$ and the noise $\boldsymbol{\delta}$. F is the forward modelling used to calculate the response $\boldsymbol{d}$ associated with the model $\boldsymbol{m}$. Hence, the set of all possible models consistent with the data is $Q_\delta = \{\boldsymbol{m} \mid \boldsymbol{m} \in M \text{ and } \|F(\boldsymbol{m}) - \boldsymbol{d}\| \leq \|\boldsymbol{\delta}\| = \delta\}$. In general, the solution of the inverse problem is the minimizer of the regularizer $s(\boldsymbol{m}) = \left\|\boldsymbol{m} - \boldsymbol{m}_{apr}\right\|$ (defining the correctness set M_c [31]) that, also, belongs to Q_δ. Here, instead, the set of all possible solutions is no longer defined uniquely by δ, but rather by the intersection $Q_\delta \cap P$, in which the set P consists of the samples of the prior distribution. D is the set of all possible measurements.

Given a noise vector $\boldsymbol{\delta}$ associated to the vector of the measurements $\boldsymbol{d}$, the subset of all possible models compatible with the observed data is defined as

$$Q_\delta = \{\boldsymbol{m} \mid \boldsymbol{m} \in M \text{ and } \|F(\boldsymbol{m}) - \boldsymbol{d}\| \leq \|\boldsymbol{\delta}\| = \delta\}, \tag{2}$$

where F is the forward modelling and M is the model space. The regularizer $s(\boldsymbol{m})$ selects from Q_δ the specific solution $\boldsymbol{m}$ that minimizes $s(\boldsymbol{m})$.

In the stochastic approaches, the a priori information is also provided via the selection of the appropriate prior distribution P: the samples of P are models defined in agreement with our expectations about the possible resistivity models. The stochastic solution consists of the a posteriori distribution populated by the models compatible with the prior and associated with their probability of being the actual model generating the observed data - clearly, this probability is a function of their corresponding data fitting.

The present approach can be considered a mixture of the deterministic and stochastic perspectives as the inversion solution is found as the minimizer $\boldsymbol{m}$ of Eq. 1 belonging at the intersection $Q_\delta \cap P$ between the prior ensemble and the set of possible models fitting the data (rather than simply at Q_δ).

In this way, we can search for the solutions (Fig. 1) with some specific (very general and arbitrarily complex) characteristics (defining the samples of P) and as close as possible to some reference models (possibly, defined by other ancillary information, consisting, for example, of the presence of 2D ERT models).

Fig. 2. The available boreholes are indicated by the large yellow, orange, and blue dots, while the EMI soundings are represented by light blue color. The ERT line is shown as a red line, and the perimeter of the area is highlighted by green dots. The coordinates are not the real ones.

In our specific case, the set P has been defined via 20×10^6 samples (consisting of 1D resistivity profiles characterized by 31 layers with logarithmically increasing thicknesses; the depth of the top of the last layer is at 30 m depth). The samples have been designed in order to be representative of the variability of the physical properties of the investigated site. Across the investigated site (Fig. 2), both EMI and ERT data have been collected. Specifically, one 2D ERT line crosses the 3D EMI survey. A portion of the result of the 2D inversion of the ERT [32] is shown in Fig. 3a. The representativeness of the EMI prior samples has been verified a posteriori by checking how well the prior samples could fit the retrieved ERT section [33]. The prior models best fitting the ERT results are shown in Fig 3b. Hence, Fig. 3c (showing the model misfit between the Fig 3a and 3b resistivity distributions) demonstrates how the typical resistivities characterizing the investigated site (Fig. 3a) can be reproduced by the possible candidates (i.e., the best fitting elements of P - in Fig. 3b) to be the solutions of the EMI inversion.

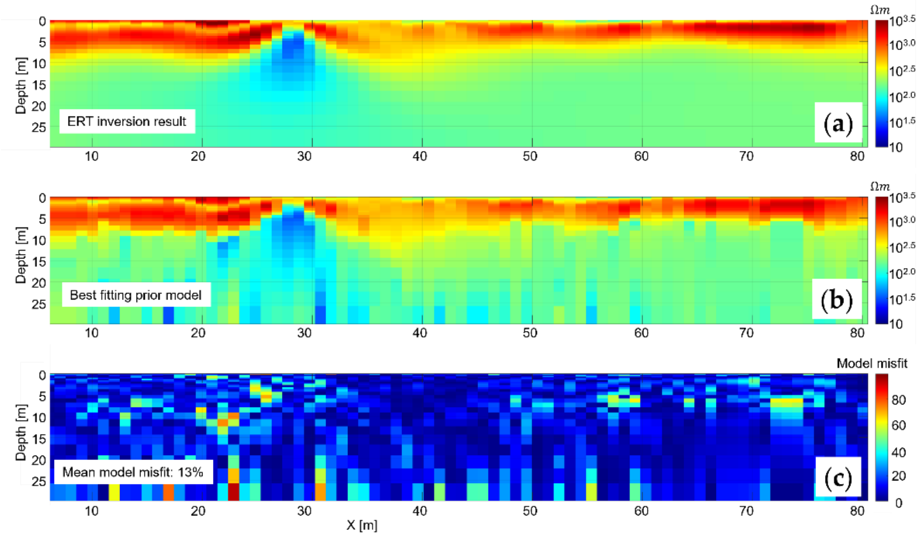

Fig. 3. Check of the prior models representativeness. (a) The 2D resistivity distribution obtained via the ERT inversion of the data along the profile crossing the investigated area (Fig. 2, red line). The only portion shown corresponds to the part overlapping the EMI survey. (b) The 2D section obtained via the best fitting 1D models of the prior distribution. (c) The percentage relative misfit between the ERT model and the best fitting one.

From an alternative perspective, the underlying logic for developing the prior is similar to creating the training datasets for machine learning applications [34]: in both cases, the sets of pairs $(\boldsymbol{m}, \boldsymbol{d})$, consisting of the prior models and the associated electromagnetic responses, and making up the training dataset, are generated based on the stationary assumption. As a result, it is essential for the pairs in the training dataset - as well as those in the prior ensemble P and its associated image in D: $F(P)$ (in Fig.1) - to be independent and identically distributed (i.i.d.) random variables [35].

Once P is populated, and the responses in $F(P)$ calculated, it is straight forward to select the models belonging to the subset $P \cap Q_\delta$ and whose data are compatible with the field observations. Subsequently, the model of the intersection $P \cap Q_\delta$ which is also the minimizer of $s(\boldsymbol{m})$ is selected as the final solution to the inverse problem.

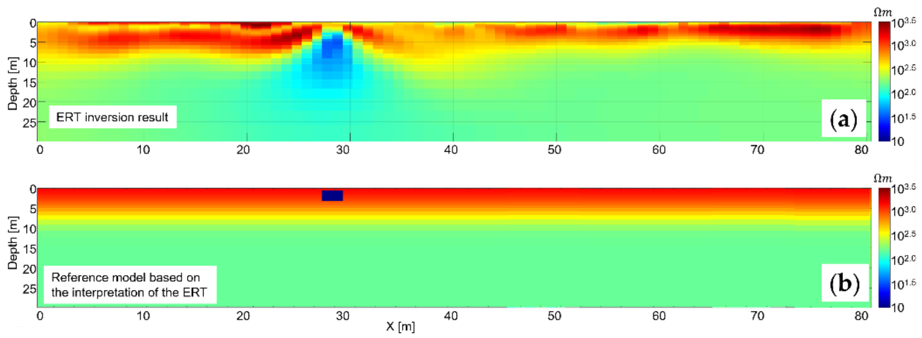

Fig. 4. The two electrical resistivity distributions used as alternative reference models for the EMI inversion. (a) The 2D resistivity from the ERT data (Fig. 2, red line, and Fig. 3a). (b) The interpretation of the ERT result.

The proposed method can be viewed as a progression from the standard spatially constrained inversion technique [6, 14]. Unlike the former, the vertical regularization in the proposed strategy is not confined to a mere demand for maximum smoothness. Instead, in this new approach, vertical spatial coherence is ensured by the selected model being an element of the prior ensemble P. Therefore, the similarity to the spatially constrained inversion concerns only the formalization of lateral constraints, opening up the possibility of reconstructing much more realistic geological structures (consistent with the prior knowledge). Of course, whereas the EMI survey profiles adjacent to the ERT section (or, in general, to any other available source of prior information) are directly constrained by the ERT resistivity values, the EMI profiles that are further distant from the ERT section are uniquely bound to the closest EMI profiles. Thus, during the EMI inversion process, moving away from the ERT section, the influence of the initial ERT information competes with the one provided by the EMI measurements themselves, and gradually weakens. This is coherent with the expectation that, as we move away from the ERT section, there would be a reduced resemblance between the electrical and electromagnetic outcomes.

From a computational perspective, the proposed method is only seemingly costly. In reality, for comparable geological settings, the elements of P can be pre-computed, and, since the forward response is independent for each 1D model, the process is highly parallelizable. Furthermore, all the challenges associated with minimizing the objective function of standard deterministic approaches (such as selecting Tikhonov's parameter [36]) are automatically eliminated and everything is reduced to simply calculating the norm of the model distance with respect to $\boldsymbol{m}_{apr}$ (Eq. 1).

In the following, we investigate the possibility to use, to guide the inversion, not just the ERT result, but, as an alternative, its interpretation based on additional information. So, we will check the consequences of using the resistivity section in Fig. 4b and compare that result against the one obtained via the distribution in Fig. 4a.

3 Results

The field data available on the test site consist of:

— the EMI dataset acquired with a Profiler EMP-400, produced by GSSI [37, 38], at frequencies: 5 KHz, 10 KHz, and 15 KHz. The EMI equipment was calibrated on-site following the standard manufacturer's prescription.

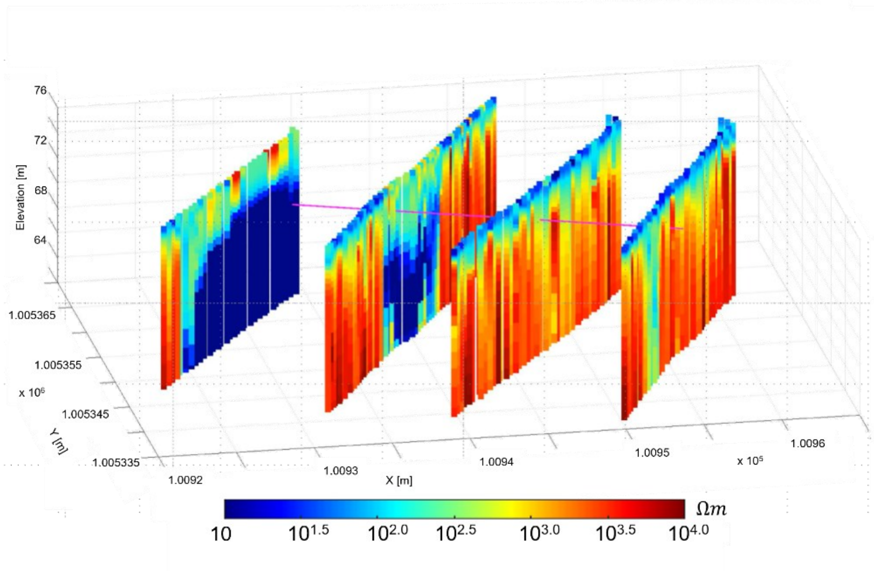

Fig. 5. Vertical slices of the 3D EMI unconstrained inversion. The purple solid line indicates where the probable pipeline's location.

— an ERT line passing, in the middle, the EMI survey area (red line in Fig. 2). The ERT was performed with a Terrameter LS2 (GuidelineGeo), with 81 electrodes 1 m apart. The acquisition protocol was a gradient nested array producing 1603 individual measurements. The contact electrical resistance was always less than 1 KΩ. The ERT inversion was performed utilizing pyGIMLi [39] and, e.g., it is shown in Fig. 4a (just the portion overlapping the EMI survey area). In that Figure, at around X = 29 m, the conductive evidence of an existing pipe is clear.

In the following, we compare the EMI inversion results, respectively:

— relying uniquely on the data and the information provided by the prior distribution (Fig. 5). In what follows, we will refer to this result as the Unconstrained result.
— incorporating the information from the 2D ERT section (Fig. 6). We call this result the ERT-constrained result.
— based on the interpretation of the ERT section as it is shown in Fig. 4b. We generally call it Model-constrained result (Fig. 7).

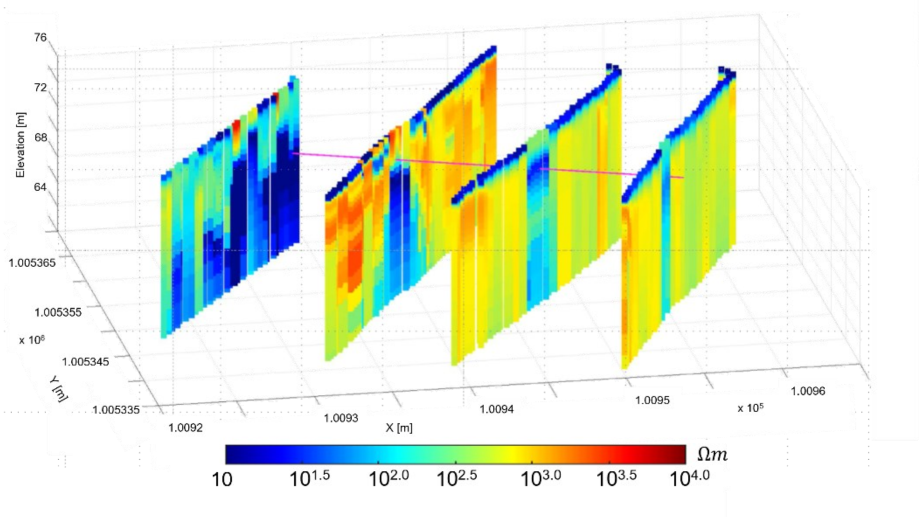

Fig. 6. The EMI ERT-constrained inversion (Fig.s 2a and 3a). The purple solid line indicates the supposed pipeline's location.

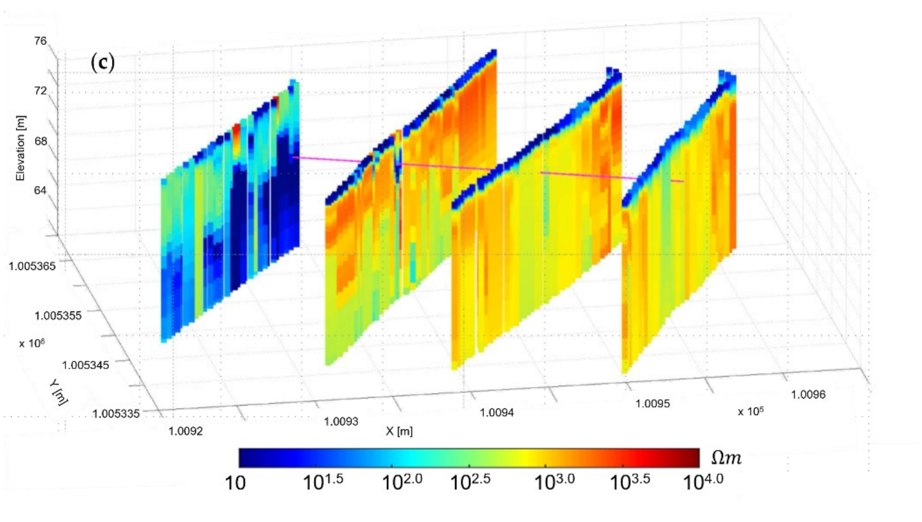

Fig. 7. The EMI Model-constrained inversion (Fig. 3b). The purple solid line indicates the supposed pipeline's location.

By comparing Fig.s 5-7, it is easy to notice that incorporating the additional information either from the ERT section or its interpretation generates results that are more spatially coherent, decreasing the spurious variations between different adjacent 1D models, which are characterizing the Unconstrained result.

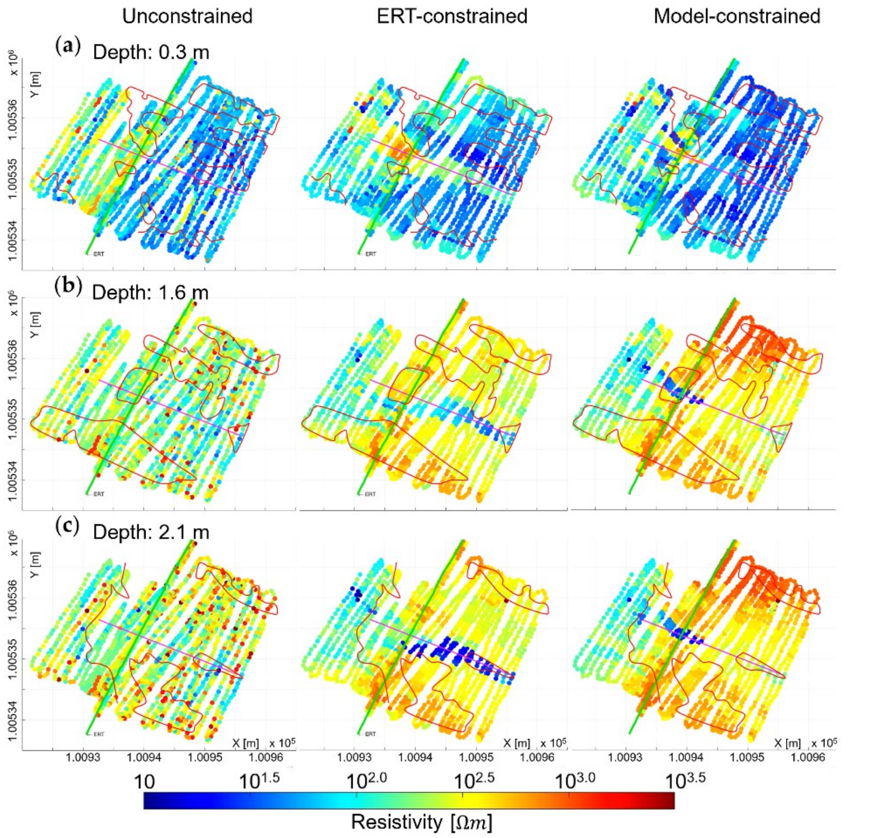

Fig. 8. Horizontal sections of the resistivity volumes obtained with different constraining strategies (Fig.s 5-7). Each row corresponds to a different depth: (a) 0.3 m; (b) 1.6 m; (c) 2.1 m. The location of the ERT section (and its geoelectrical interpretation) is shown as a green solid line. The assumed position of the pipe is plotted in purple. The red contours are shown as references to the anomalies; their purpose is merely to make the comparisons easier, and they are not necessarily connected to any specific geological features.

Possibly, this fact is even more evident when checking the horizontal slices at different depths of the (pseudo-)3D EMI volumes as in Fig.s 8-9. In particular, the ERT- and Model-constrained results in Fig.s 8-9 highlight clearly the presence of the non-metallic pipe known to be crossing the area (whose location is shown in Fig.s 8-9 as a purple solid line). The presence of the pipeline at around 2.4 m depth is confirmed by means of other investigations.

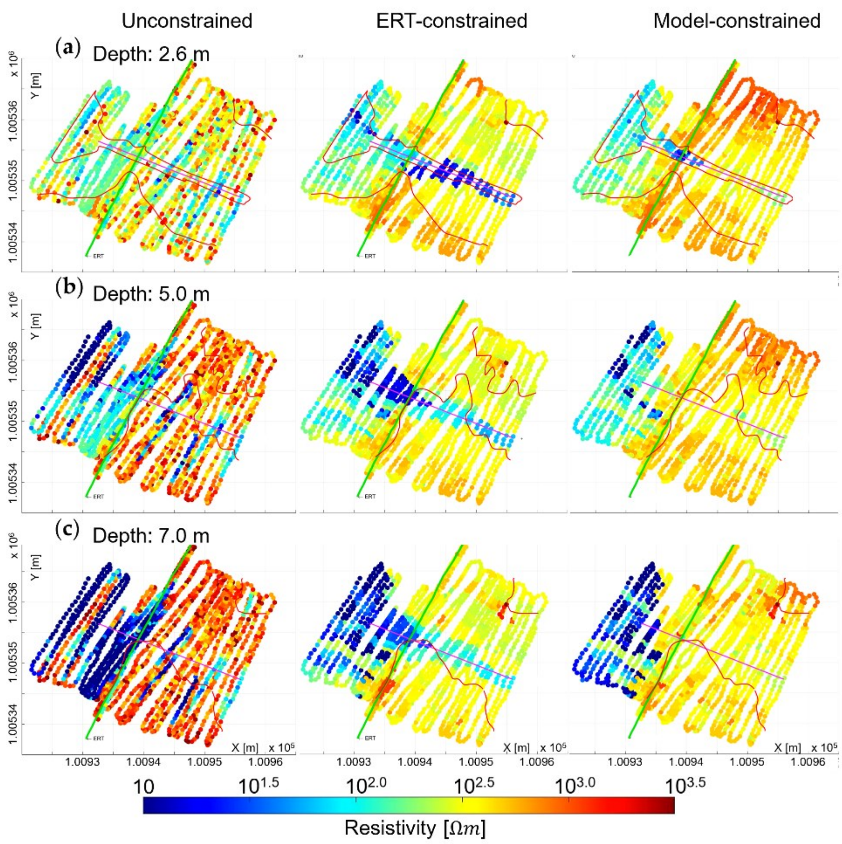

Fig. 9. Horizontal sections of the resistivity volumes obtained with different constraining strategies (Fig.s 5-7). Each row corresponds to a different depth: (a) 2.6 m; (b) 5.0 m; (c) 7.0 m. The location of the ERT section (and its geoelectrical interpretation) is shown as a green solid line. The assumed position of the pipe is plotted in purple. The red contours are shown as references to the anomalies; their purpose is merely to make the comparisons easier, and they are not necessarily connected to any specific geological features.

The Model-constrained inversion seems to better retrieve the actual resistivity distribution even compared against the ERT-constrained result as the pipe reconstruction is more coherent with its most probable location; in this respect, for example, in Fig.s 9b-c, the Model-constrained reconstruction shows no traces of the conductive pipe deeper than 2.6 m (where, indeed, it should not appear since it is shallower than that).

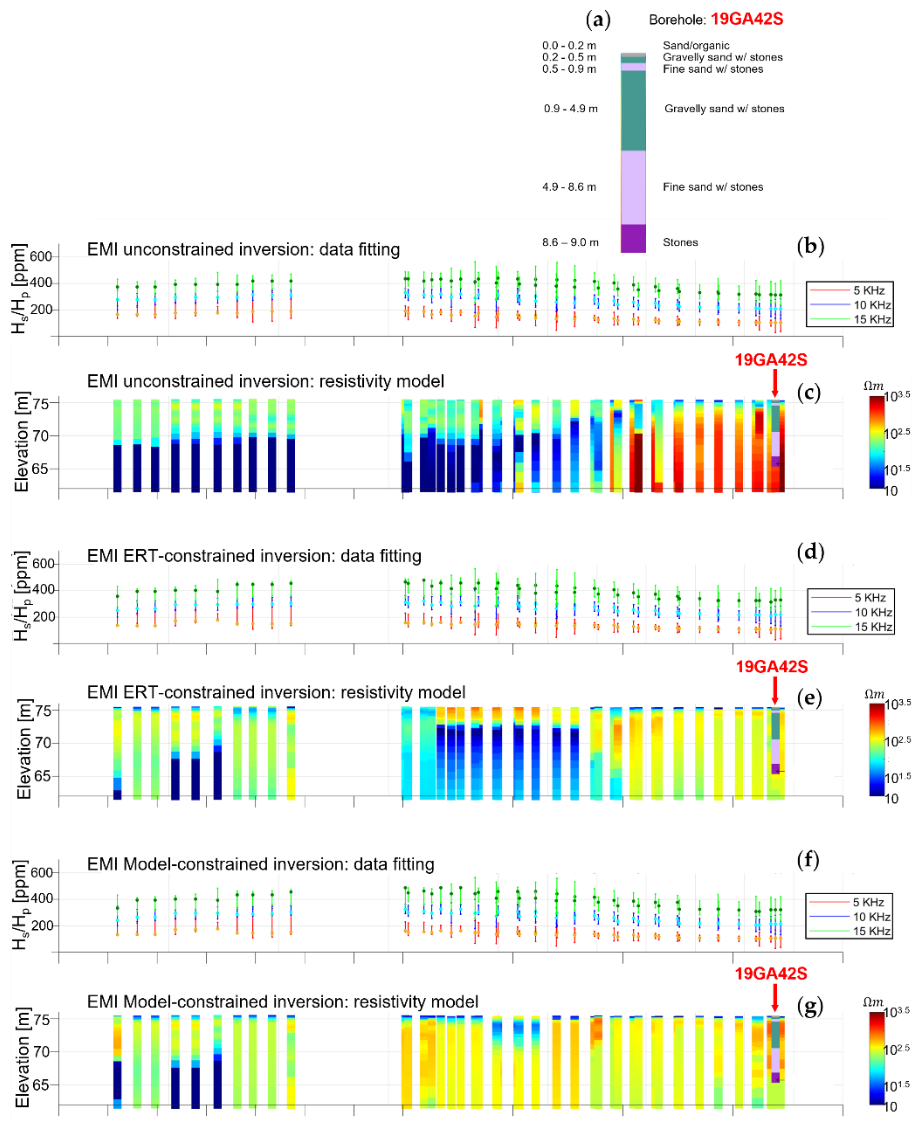

Fig. 10. Vertical sections of the EMI inversions performed by utilizing different ancillary information. (a) Description of borehole no. 19GA42S (Fig. 1). (b-c) Data fitting and model for the Unconstrained inversion. (d-e) Data fitting and model for the ERT-constrained in-version. (f-g) Data fitting and model for the Model-constrained inversion.

In addition to the verification against the pipeline presence and location, the vertical sections of the retrieved EMI volumes have been checked also against the available borehole logs, whose locations are plotted in Fig. 1 (c.f. the yellow, orange, and blue large dots [40]).

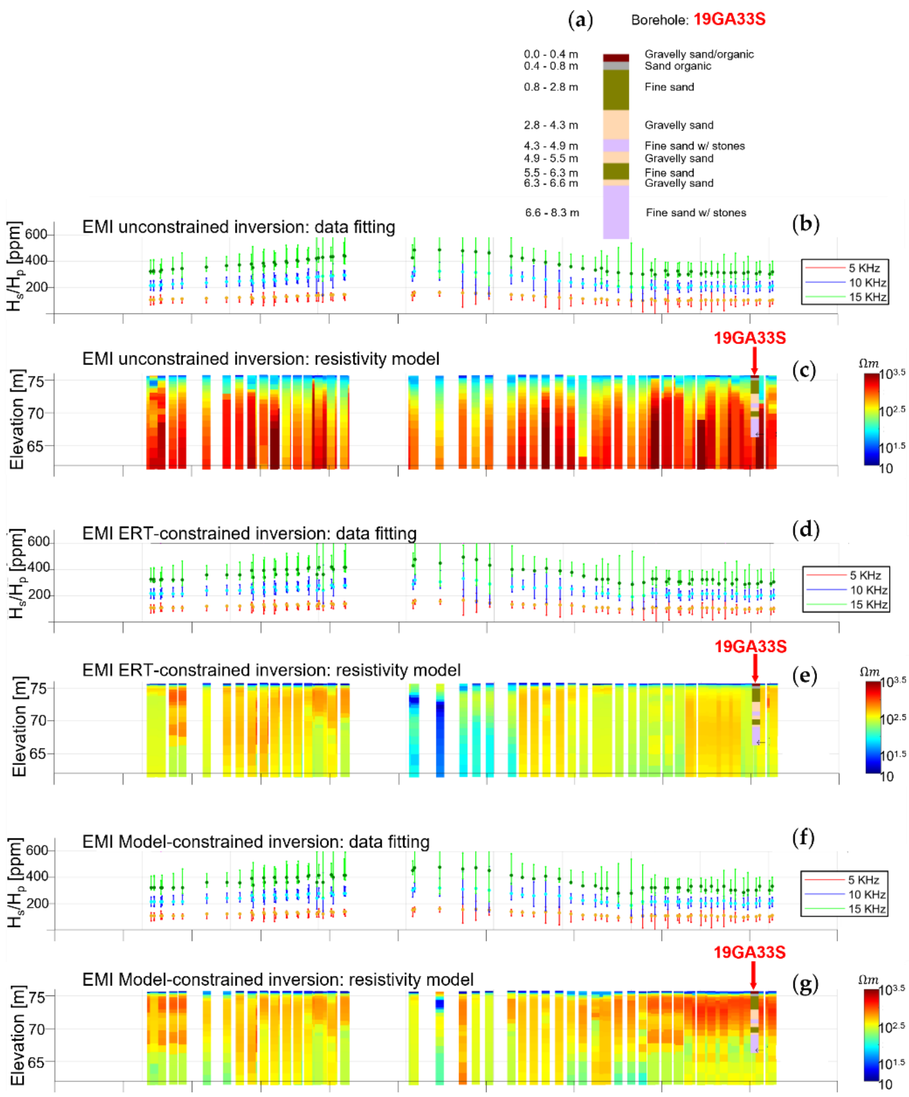

Fig. 11. Vertical sections of the EMI inversions performed by utilizing different ancillary information. (a) Description of borehole no. 19GA33S (Fig. 1). (b-c) Data fitting and model for the Unconstrained inversion. (d-e) Data fitting and model for the ERT-constrained in-version. (f-g) Data fitting and model for the Model-constrained inversion.

On this matter, Fig.10 shows the vertical sections of the three 3D EMI inversions are compared against the corresponding stratigraphy of the nearest borehole (19GA42S): these significantly different results further demonstrate the necessity of including the proper ancillary information during the inversion; also the ERT- and Model-constrained results are quite different (Fig.s 10e and g) even if the data fitting is clearly equally good for all the cases (Fig.s 10b, d, and f). Furthermore, concerning the borehole stratigraphy, not only the EMI results can match the conductive shallow layers in the well, but the Model-constrained inversion can correctly identify the interface at 8.6 m depth visible in the log.

Analogous conclusions can be drawn from the other vertical section in Fig. 11, associated with the borehole 19GA33S. Also here, the three EMI inversions are significantly different. And, whereas the ERT-constrained reconstruction shows (in agreement with its constraint - Fig. 4a), in the center of the section, a deep conductive unit, the Model-constrained inversion is characterized by a sharper conductive anomaly (again, in accordance with the information - concerning a blocky square conductive body embedded in a laterally homogeneous background - characterizing the adopted reference model in Fig. 4b). Also in this case, the features in Fig. 11g match more effectively the interface at 6.6 m depth noticeable in the borehole.

4 Conclusions

The approach we propose here concerns a novel strategy for the 3D inversion of EMI data making use of:

- a 1D forward modelling;
- a realistic (arbitrarily complex) prior, conditioning the results along the vertical direction;
- the availability of additional sources of information (e.g., in the form of 2D ERT reconstructions or 2D geological sections crossing the area in which the EMI measurements have been collected) capable to guarantee the desired level of lateral coherence in the final resistivity volume.

Through a field example, and by comparing the obtained EMI outcome against the evidence from boreholes and the preexisting knowledge concerning a non-metallic pipeline present in the investigated area, we demonstrate the effectiveness of our approach in spreading the information available in portions of the area across the entire volume, and in doing that while incorporating additional a priori information via the selection of the appropriate prior distribution models.

The new approach is only apparently expensive from a computational perspective. In reality, since each response of the 1D samples of the prior can be calculated independently, our approach is massively parallelizable, moreover, it is immune from all the numerical issues connected with the minimization of the objective functional. In addition, the same prior (and its associated responses) can be pre-calculated for areas that are geologically similar (i.e., that are, statistically speaking, stationary); this possibility makes the inversion of the datasets collected over similar settings extremely efficient.

Acknowledgments

The authors are very grateful to Dr. Henning Persson (Geological Survey of Sweden, SGU) for his support during the survey and for providing the background material. In addition, many thanks are due to the Engineering Geology Division of Lund University for its logistical support.

References

1. Guillemoteau, J., Christensen, N. B., Jacobsen, B. H., Tronicke, J.: Fast 3D multichannel deconvolution of electromagnetic induction loop-loop apparent conductivity data sets acquired at low induction numbers. Geophysics, 82(6), E357-E369 (2017).
2. Koganti, T., Van De Vijver, E., Allred, B. J., Greve, M. H., Ringgaard, J., Iversen, B. V.: Mapping of agricultural subsurface drainage systems using a frequency-domain ground penetrating radar and evaluating its performance using a single-frequency multi-receiver electromagnetic induction instrument. Sensors, 20(14), 3922 (2020).
3. Karshakov, E. V., Podmogov, Y. G., Kertsman, V. M., Moilanen, J.: Combined Frequency Domain and Time Domain Airborne Data for Environmental and Engineering Challenges. Journal of Environmental and Engineering Geophysics, 22(1), 1-11 (2017).
4. Yin, C., Hodges, G.: 3D animated visualization of EM diffusion for a frequency-domain helicopter EM system. Geophysics, 72(1), F1-F7 (2007).
5. Won, I. J., Oren, A., & Funak, F.: GEM-2A: A programmable broadband helicopter-towed electromagnetic sensorGEM-2A HEM Sensor. Geophysics, 68(6), 1888-1895 (2003).
6. Dzikunoo, E. A., Vignoli, G., Jørgensen, F., Yidana, S. M., Banoeng-Yakubo, B.: New regional stratigraphic insights from a 3D geological model of the Nasia sub-basin, Ghana, developed for hydrogeological purposes and based on reprocessed B-field data originally collected for mineral exploration. Solid Earth, 11(2), 349-361 (2020).
7. Thiesson, J., Kessouri, P., Schamper, C., Tabbagh, A.: Calibration of frequency-domain electromagnetic devices used in near-surface surveying. Near Surface Geophysics, 12(4), 481-491 (2014).
8. Foged, N., Auken, E., Christiansen, A. V., Sørensen, K. I.: Test-site calibration and validation of airborne and ground-based TEM systems. Geophysics, 78(2), E95-E106 (2013).
9. Ley-Cooper, Y., Macnae, J., Robb, T., Vrbancich, J.: Identification of calibration errors in helicopter electromagnetic (HEM) data through transform to the altitude-corrected phase-amplitude domain. Geophysics, 71(2), G27-G34 (2006).
10. Triantafilis, J., Laslett, G. M., McBratney, A. B.: Calibrating an electromagnetic induction instrument to measure salinity in soil under irrigated cotton. Soil Science Society of America Journal, 64(3), 1009-1017 (2000).
11. Minsley, B. J., Smith, B. D., Hammack, R., Sams, J. I., Veloski, G.: Calibration and filtering strategies for frequency domain electromagnetic data. Journal of Applied Geophysics, 80, 56-66 (2012).
12. Bai, P., Vignoli, G., Hansen, T. M.: 1D stochastic inversion of airborne time-domain electromagnetic data with realistic prior and accounting for the forward modeling error, Remote Sensing, 13(19), 3881 (2021).
13. Hansen, T. M., Cordua, K. S., Jacobsen, B. H., Mosegaard, K. Accounting for imperfect forward modeling in geophysical inverse problems—exemplified for crosshole tomography, Geophysics, 79(3), H1-H21 (2014).

14. Viezzoli, A., Auken, E., Munday, T.: Spatially constrained inversion for quasi 3D modelling of airborne electromagnetic data–an application for environmental assessment in the Lower Murray Region of South Australia. Exploration Geophysics, 40(2), 173-183 (2009).
15. Brodie, R., Sambridge, M.: A holistic approach to inversion of frequency-domain airborne EM data. Geophysics, 71(6), G301-G312 (2006).
16. McLachlan, P., Blanchy, G., Binley, A. EMagPy: open-source standalone software for processing, forward modeling and inversion of electromagnetic induction data, Computers & Geosciences, 146, 104561 (2021).
17. Vignoli, G., Fiandaca, G., Christiansen, A. V., Kirkegaard, C., Auken, E.: Sharp spatially constrained inversion with applications to transient electromagnetic data. Geophysical Prospecting, 63(1), 243-255 (2015).
18. Klose, T., Guillemoteau, J., Vignoli, G., Tronicke, J. Laterally constrained inversion (LCI) of multi-configuration EMI data with tunable sharpness, Journal of Applied Geophysics, 196, 104519 (2022).
19. Vignoli, G., Sapia, V., Menghini, A., Viezzoli, A. Examples of improved inversion of different airborne electromagnetic datasets via sharp regularization, Journal of Environmental and Engineering Geophysics, 22(1), 51-61 (2017).
20. Ley-Cooper, A. Y., Viezzoli, A., Guillemoteau, J., Vignoli, G., Macnae, J., Cox, L., Munday, T. Airborne electromagnetic modelling options and their consequences in target definition, Exploration Geophysics, 46(1), 74-84 (2015).
21. Klose, T., Guillemoteau, J., Vignoli, G., Walter, J., Herrmann, A., Tronicke, J.: Structurally constrained inversion by means of a Minimum Gradient Support regularizer: examples of FD-EMI data inversion constrained by GPR reflection data. Geophysical Journal International. 233(3), 1938-1949 (2023).
22. Pagliara, G., Vignoli, G.: Focusing inversion techniques applied to electrical resistance tomography in an experimental tank. In: XI International Congress Proceedings of the International Association for Mathematical Geology, Liege, Belgium (2006).
23. Thibaut, R., Kremer, T., Royen, A., Ngun, B. K., Nguyen, F., Hermans, T.: A new workflow to incorporate prior information in minimum gradient support (MGS) inversion of electrical resistivity and induced polarization data. Journal of Applied Geophysics, 187, 104286 (2021).
24. Fiandaca, G., Doetsch, J., Vignoli, G., Auken, E. Generalized focusing of time-lapse changes with applications to direct current and time-domain induced polarization inversions, Geophysical Journal International, 203(2), 1101-1112 (2015).
25. Karaoulis, M., Revil, A., Tsourlos, P., Werkema, D. D., Minsley, B. J. IP4DI: A software for time-lapse 2D/3D DC-resistivity and induced polarization tomography, Computers & Geosciences, 54, 164-170 (2013).
26. Zhou, J., Revil, A., Karaoulis, M., Hale, D., Doetsch, J., Cuttler, S.: Image-guided inversion of electrical resistivity data. Geophysical Journal International. 197(1), 292-309 (2014).
27. Vignoli, G., Guillemoteau, J., Barreto, J., Rossi, M.: Reconstruction, with tunable sparsity levels, of shear wave velocity profiles from surface wave data. Geophysical Journal International, 225(3), 1935-1951 (2021).
28. Hansen, T. M.: Efficient probabilistic inversion using the rejection sampler - exemplified on airborne EM data. Geophysical Journal International, 224(1), 543-557 (2021).
29. Hansen, T. M., Minsley, B. J.: Inversion of airborne EM data with an explicit choice of prior model. Geophysical Journal International, 218(2), 1348-1366 (2019).
30. Mosegaard, K., Tarantola, A.: Monte Carlo sampling of solutions to inverse problems, Journal of Geophysical Research: Solid Earth, 100(B7), 12431-12447 (1995).

31. Tikhonov, A. N., Arsenin V. Y.: Solutions of ill-posed problems, 1st ed.; V. H. Winston & Sons: Washington, U.S.A. (1977).
32. Rücker, C., Günther, T., Wagner, F. M.: pyGIMLi: An open-source library for modelling and inversion in geophysics. Computers & Geosciences, 109, 106-123 (2017).
33. Høyer, A. S., Vignoli, G., Hansen, T. M., Vu, L. T., Keefer, D. A., Jørgensen, F.: Multiple-point statistical simulation for hydrogeological models: 3-D training image development and conditioning strategies. Hydrology and Earth System Sciences, 21(12), 6069-6089 (2017).
34. Bai, P., Vignoli, G., Viezzoli, A., Nevalainen, J., Vacca, G.: (Quasi-) real-time inversion of airborne time-domain electromagnetic data via artificial neural network. Remote Sensing, 12(20), 3440 (2020).
35. Neal, R.M.: Bayesian learning for neural networks (Vol. 118). Springer Science & Business Media, Berlin, Germany (2012).
36. Zhdanov, M. S., Vignoli, G., Ueda, T.: Sharp boundary inversion in crosswell travel-time tomography. Journal of Geophysics and Engineering, 3(2), 122-134 (2006).
37. Haynie, K. L., Khan, S. D.: Shallow subsurface detection of buried weathered hydrocarbons using GPR and EMI. Marine and Petroleum Geology, 77, 116-123 (2016).
38. Rashed, M., Niyazi, B. Environmental impact assessment of the former Al-Musk lake wastewater dumpsite using electromagnetic induction technique. Earth Systems and Environment, 1(1), 1-10 (2017).
39. Rücker, C., Günther, T., Wagner, F. M.: pyGIMLi: An open-source library for modelling and inversion in geophysics. *Computers & Geosciences*, 109, 106-123 (2017).
40. Torin L., Davidsson L., Nilsson M.: Inledande projektering av Nisses kemtvätt i Osby. Report for Sveriges Geologiska Undersökning by WSP Environmental Sverige, Sweden (2021).